The final publication is available at

https://doi.org/10.1016/j.matchar.2020.110286

Additional Information

Single step heat treatment for the development of beta titanium composites with in-situ TiB and TiC reinforcement

Vitor V. Rielli[a], Vicente Amigó-Borrás[b], Rodrigo J. Contieri[a,*]

[a] *University of Campinas, School of Applied Sciences, 13484-350 Limeira, Brazil*

[b] *Institute of Materials Technology, Universitat Politècnica de València, 22012, Valencia, Spain*

ABSTRACT

Titanium matrix composites have been attracting great interest from aerospace industry due to favorable properties like thermal stability, high specific strength, corrosion, and wear resistance. Optimal relation between mechanical properties demands complex processing routes and, in this context, the effects of a single-step processing route on microstructure and mechanical properties of β titanium matrix composites was placed on focus in this study. The commercial TIMETAL Beta 21S alloy and its modification with the addition of B_4C were developed, allowing in-situ formation of TiB and TiC particles in a β matrix. The composites presented highest values of mechanical strength and hardness, and the addition of 3% of B_4C provided a significant reduction in grain size, and compressive yield strength and ultimate compressive strength values of 1205 MPa and 1636 MPa, respectively, with a maximum deformation of 20.5%. An orientation relationship investigation provided in- formation about some unconventional relation between the present phases.

1. Introduction

Titanium matrix composites with discontinuous in-situ reinforce- ments have recently attracted great attention due to a wide range of possible properties, allowing a great diversity of applications, especially in the aerospace industry, where strict requirements of thermal stabi- lity, high specific strength, corrosion, and wear resistance may be present [1–3]. Beta 21S (Ti-15Mo-3Nb-3Al-0.2Si, wt%) is a titanium alloy developed as a suitable matrix material for composites, being resistant to highly oxidizing and corrosive environments at elevated temperatures, as in sections of an aircraft engines, such as the plug-and- nozzle [4]. Additions of B and C, separately, in Beta 21S at low con- centrations, have been subject of previous researches, which demonstrated the effects on grain refinement, α precipitation, and mechanical properties changes [5–7], due to TiB or TiC formation. Other β metastable alloys, such as Ti-15Mo, Ti-15-3, Ti-5533, with B, C, or B_4C additions have also been previously investigated [8–11], which shows the

increasing interest in developing β Ti matrix composites with these types of reinforcements.

The synthesis of thermodynamically stable in-situ reinforcements, such as TiB and TiC in β titanium matrix, increases strength and hardness, but ductility decreases depending on the volume of pre- cipitates. The ductility decrement can be affected on a smaller degree with heat treatments and formation of fine α phase, where the cooling rate from temperatures above β transus plays an important role on the final morphology of α precipitates, as equiaxial shape has been reported after slow cooling of titanium matrix composites based on Ti-6Al-4V, needle-like shape [12,13], and Widmanstätten colonies have also been reported after aging [14].

On one hand, the presence of substoichiometric carbides seems to refine α precipitates due to gettering of oxygen from the matrix, de- creasing formation of detrimental grain boundary α phase [15]. Borides, on the other hand, have shown to act as nucleation sites for α, improving homogeneous distribution [16].

Mechanical properties are also modified by β grain refinement, and TiB and TiC have been widely studied as effective restraining particles for grain boundaries mobility in high temperature treatments, through the mechanism of Zener pinning [17–19]. However, conventional processing routes of cast β titanium alloys involve homogenization, hot or cold deformation, annealing, and aging [20], while a single-step heat treatment yielding good relation between strength and ductility would be very desirable due to decreases in production cost and time. Thus, from the development of a β-type titanium metal matrix composites through the incorporation of TiB and TiC in Beta 21S by in-situ reac- tions, the present study aims to propose a new processing route, from the as-cast condition followed by annealing solution in a single-step. Potential benefits for the aerospace industry would include reductions in manufacturing costs of a newly developed composite with improved mechanical properties in comparison to the alloy, allowing a range of new applications in more mechanically demanding sections of aircraft engines.

Table 1 Nominal composition of the materials (wt%).

Material	Nominal composition (wt%)						
	Mo	Nb	Al	Si	B	C	Ti
FC 0	15	3	3	0.2	0	0	Balance
FC 0.5					0.4	0.1	
FC 1.5					1.2	0.3	
FC 3					2.4	0.6	

Complementarily, the orientation relationship (OR) between β, α, TiB and TiC is generally studied in materials with either the boride or the carbide, however, investigating the OR of these phases in a hybrid context, through EBSD and TEM-ASTAR images helps to extend the understanding of the predominant morphology of α and its nucleation sites, which impacts mechanical properties. EDS line scans show an interesting pattern of distribution of elements in the composites. In this research, the morphology and orientation relationship between each phase in materials heat treated above β transus followed by slow cooling were investigated. Effects on

microstructure refinement due to the reinforcements and mechanical properties are discussed as well.

2. Experimental procedure

Table 1 shows the nominal composition of the alloy and the composites based on the Beta 21S titanium alloy (Ti-15Mo-3Nb-3Al-0.2Si, wt%). Non-consumable tungsten electrode vacuum arc remelting furnace (VAR) was employed as fabrication technique and due to the small dimensions of the ingots, around 100 mm, and total mass of 70 g, high cooling rates are expected as most parts of the ingots are in close contact with the water-cooled Cu crucible. Each element was added in its pure elemental form while boron and carbon were added as B_4C powder (98% purity). Ingots were remelted at least five times to ensure complete homogenization.

The chosen compositions of B and C as displayed in Table 1 are hypoeutectic, near-eutectic, and hypereutectic for FC 0.5, FC 1.5 and FC 3, respectively, as the eutectic composition of C is 0.4 wt% in Ti-CP [21], and the eutectic composition of B in pure Ti is close to 1.6 wt% [22] and 1.55 wt% in Ti-6Al-4V [23], which shows the susceptibility to variations owing to the presence of elements in solid solution.

The small difference of density between Ti (4.57 g/cm^3) and TiB (4.56 g/cm^3), and coefficient of thermal expansion (CTE) ($CTE_{Ti} = 8.6 \times 10^{-6}$ K^{-1}, and $CTE_{TiB} = 7.15 \times 10^{-6}$ K^{-1}) [24], makes it a viable discontinuous reinforcement for titanium because residual stress is minimized in the composite after the in-situ reaction [25]. TiC also offers attractive properties as reinforcement for titanium matrix composites, as TiC density (4.92 g/cm^3) is only 7% higher than Ti and its CTE is even closer to Ti than TiB ($CTE_{TiC} = 7.95 \times 10^{-6}$ $°K^{-1}$) [24]. It should be noted that the aforementioned values of eutectic composition as well as the overall density and CTE of the titanium matrix may be altered by alloying elements such as Mo, Al, and Nb.

Samples were cut from the central portion of each ingot and heat treated in inert atmosphere of Ar above β transus (~815 °C for Beta 21S) [26] at 1000 °C for 12 h, then furnace cooled (FC) (3 °C/min).

For SEM and EBSD, samples were hot mounted in Bakelite resin with carbon filler, then grinded with SiC grinding paper with pro- gressive grit size from 80 to 1200 followed by fine grinding with an MD- Largo disc with 9 μm diamond suspension. Polishing was carried out on a porous neoprene polishing cloth on 90% colloidal silica/10% H_2O_2 suspension with final polishing for 6 h on a vibratory polisher in col- loidal silica suspension. Backscattered SEM images were acquired on a FEI Quanta 650 FEG, while EDS analysis and EBSD maps were obtained on a ZEISS Auriga Compact. A PANalytical X'Pert diffractometer with Cu-Kα (λ = 0.15406 nm) at 40 kV and 30 mA was used for X-ray diffraction on polished samples.

TEM samples were first cut from the ingots with approximately 300 μm of thickness, followed by grinding up to 100 μm. Disks with 3 mm of diameter were obtained with a specimen punch tool and a lamella was produced through focused ion beam (FIB) milling on a ZEISS Auriga Compact, gradually decreasing voltage to minimize damaged layers. TEM observations were made on a 200-kV field emission JEOL JEM-2100F. TEM orientation imaging was performed with ASTAR™ from NanoMEGAS.

For each composition, cylindrical specimens with 3 mm of diameter and 6 mm of height were cut by electric discharge machining for compression tests following the specifications of ASTM E9-09 [27], which were carried out at a strain rate of 0.01 s^{-1} at room temperature on an MTS electromechanical universal testing system. The average values of three compression tests for each material were obtained.

Vickers microhardness was measured with a testing force of 4.9 N (HV 0.5) on a Shimadzu tester HMV-FA2. Macrohardness was measured with a load of 98 N (HV 10) on a Centaur hardness tester (HD9-45). Macroindentations were measured on an optical microscope (Nikon Eclipse LV100). For both micro and macrohardness, indentation was performed during 10 s in 10 different positions on the sample.

3. Results

3.1 Microstructural analysis

Fig. 1 shows X-ray diffraction patterns of the materials after heat treatment. FC 0 has only α and β peaks, while the addition of 0.5 wt% of B_4C creates enough volume of TiB and TiC to make visible peaks in the region shown in the inset. FC 0.5 also has peaks of α and β, however, peaks of the former phase seem to decrease in intensity as com- pared to FC 0. This reduction trend is confirmed for FC 1.5, where the $(101)_\alpha$ peak is the only one that can be clearly identified as belonging to α, while the remaining α peaks overlap with TiB peaks, such as $(112)_{TiB}$ and $(122)_{TiB}$. On the other hand, the increase in the intensity of peaks of TiB and TiC is clear from FC 0.5 to FC 1.5, increasing even more for FC 3, which besides those, only has β peaks, verifying the trend of α re- duction with B_4C addition, and the consequent increase in volume of TiB and TiC.

Fig. 1. X-ray diffraction patterns of Beta 21S alloy and composites. Inset shows the 2θ region from
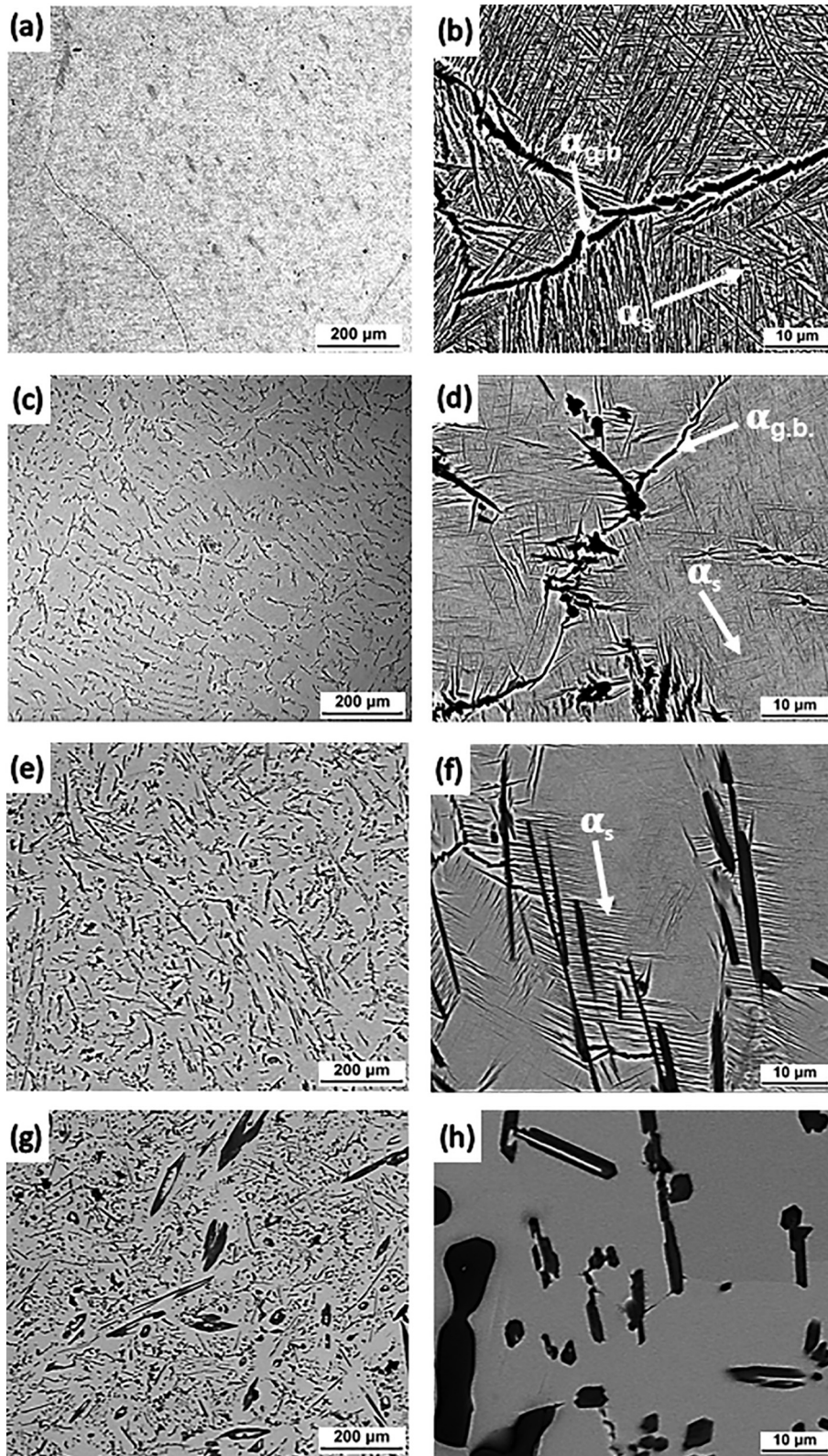

35° to 43°.
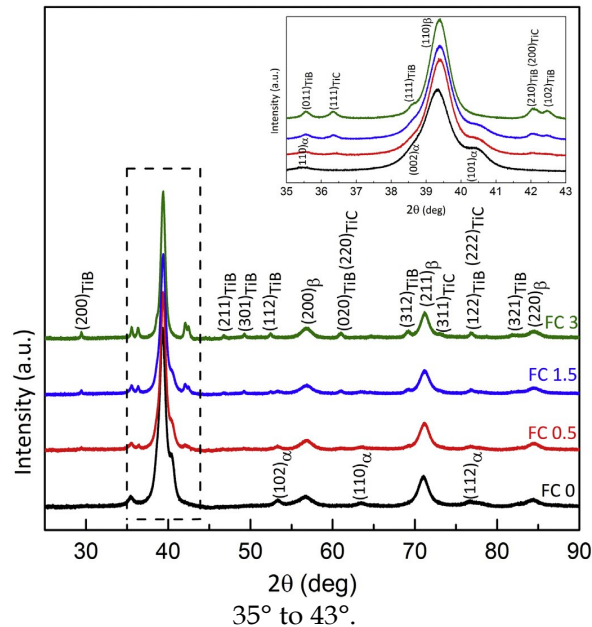
Fig. 2. Backscattered SEM micrographs of furnace cooled materials. (a–b) FC 0; (c–d) FC 0.5; (e–f) FC 1.5; (g–h) FC 3.

Fig. 2 shows the microstructure of the alloy and composites. The cooling rate from above β

transus, inside the furnace, is slow enough to transform β to α in FC 0, as shown in Fig. 2a. In Fig. 2b, grain boundary α ($\alpha_{g.b}$) is coarser than all the remaining secondary α (α_s) inside prior β grains, which means they formed first during cooling, agreeing with the TTT developed by Imam [28]. Adding 0.5 wt% of B_4C creates a dendritic distribution of dark particles as shown in Fig. 2c, which are mainly TiB, but TiC is also present, as confirmed later with EBSD images. Fig. 2d shows that $\alpha_{g.b}$ and α_s have been refined with the presence of TiB and TiC, as confirmed by X-ray diffraction. In Fig. 2e, of FC 1.5, there is a larger volume of dark particles, but none are ex- tremely coarse, as those seen in Fig. 2g, meaning that primary phases of TiC and TiB were only formed in FC 3. The α phase volume decreased for higher additions of B_4C, as seen for FC 1.5 in Fig. 2f, where fine needle-like α_s, indicated by the white arrow, seems to have grown from the dark precipitates, which are possibly whiskers of TiB. Finally, Fig. 2h shows that at the same magnification of the previous images, none α can be identified.
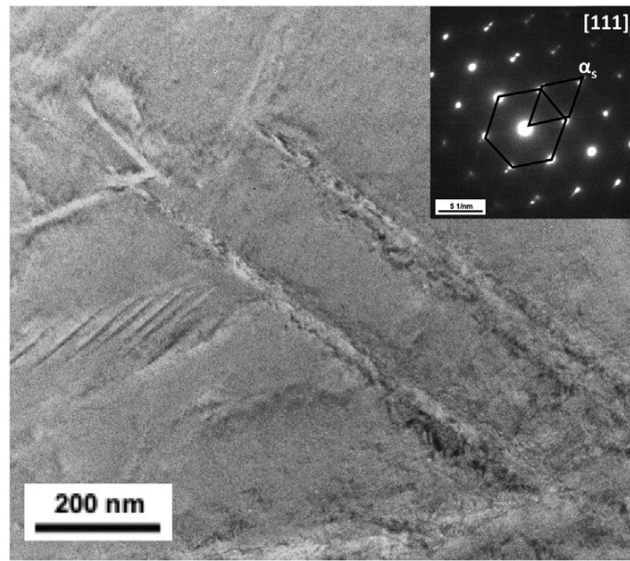

Fig. 3. TEM image of FC 3 showing needle-like α in a matrix of β, as confirmed by SAD in the inset.

In Fig. 3, needle-like α is seen in a matrix of β, showing that for FC 3, α was refined to nanometric dimensions. In Fig. 4, it can be seen that long exposure to temperatures above β transus induced to extreme grain coarsening, mainly for FC 0, which has an average grain size of 1033 μm. For FC 0.5, the presence of TiB and TiC precipitates made grains size of primary β decrease to an average value of 196 μm, however, great deviation from this value occurs due to some large grains identified in the image. In this material, during solidification, primary β phase forms first and it expels B, which has negligible solubility in Ti, to the solid-liquid interface, and TiB is formed, restraining the increase in β grain size and also providing additional nucleation sites for other β grains. However, it should be pointed out that TiB and TiC particles are formed inside β grains as well, as seen in Fig. 2c, precipitates are homogenously distributed in the matrix, not only in the grain boundaries. Grain size in FC 1.5 is reduced to 150 μm as this material is considered to be near to eutectic composition for both B and C, leading to the formation of β, TiB, and TiC at the same rate from the liquid, which decreases grain growth during solidification. We assume that

the composition in this case is near eutectic because there is no phase diagram available considering all the seven main elements pre- sent in the composites, and the best reference is a Ti-B_4C isopleth [29], a Ti-C [21], and Ti-B [22] phase diagram, so it is expected some degree of variation in the eutectic composition. Even after a 12-h heat treat- ment at 1000 °C, columnar grains with ⟨001⟩ orientation are still pre- sent as seen on the right-hand side of Fig. 4c, which is a well known effect that takes place near high heat extraction zones when VAR is chosen as the melting technique [30]. At last, FC 3 grains have an average size of 24 μm, which is a quite large reduction due to the formation of primary TiB and TiC precipitates and a larger volume of smaller eutectic precipitates, that act as nucleation sites for β, as shown in Fig. 4d.
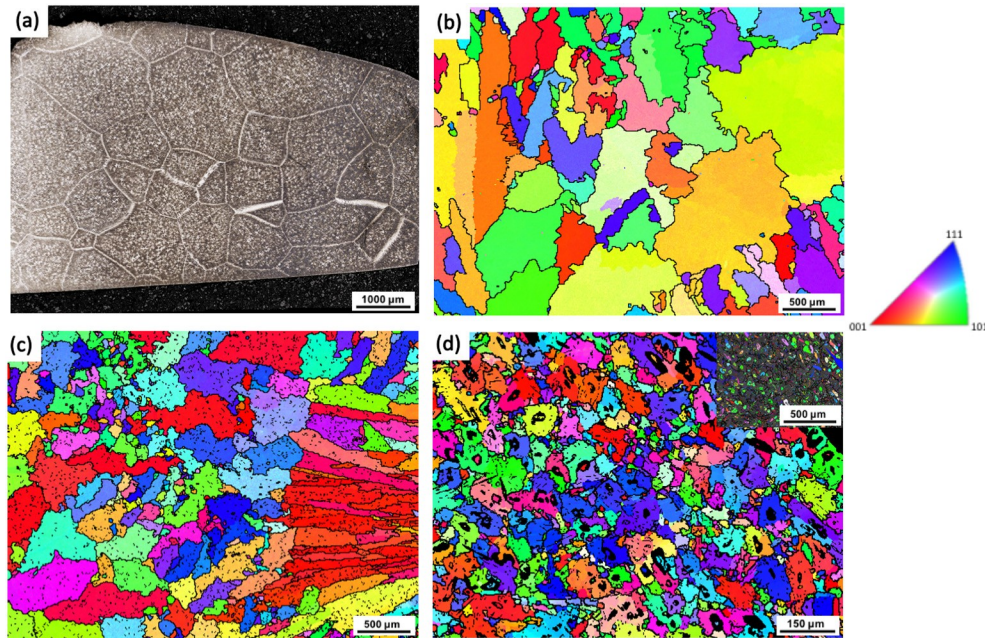

Fig. 4. (a) Optical macrostructure of FC 0 with average grain size of 1033 μm; (b–d) EBSD maps with IPF coloring scheme for (b) FC 0.5, (c) FC 1.5 and (d) FC 3, with grain sizes of 196 μm, 150 μm, and 24 μm, respectively. Inset in (d) shows in-situ precipitates.

3.2 Orientation relationship investigation

The EBSD phase map in Fig. 5 shows that due to instrument limitations, fine α in FC 0.5 could not be properly indexed as the inset image shows that there is a larger volume of α distributed in the β matrix, that is not present on the EBSD phase map. Images on the right portion of the figure have, in colors, the phases considered for each OR analysis, while other phases are portrayed in black. OR shown in the images are not the only ones possible, but are the best found by the authors.

For most interfaces between α and β, there is a low deviation degree from the common orientation relationship of {110}β || {0001}α, however, some rounded α particles attached to borides and carbides have deviations larger than 20°, which is expected when α nucleate from them. The OR of β and TiB is given by {314}β || {122}TiB , which is unusual, since no similar OR was

found in literature, and that may be caused by the rapid solidification in VAR processing, so phases did not have enough time to form a proper OR. The relationship between β and TiC is given by {113}$_β$ || {113}$_{TiC}$. In the image showing the OR be- tween α and TiB, a TiB particle completely surrounded by α shows deviation higher than 20° from the proposed OR of {1120}$_α$ || {010}$_{TiB}$, however, most of the remaining TiB shows low deviations. There is no considerable deviation between α and TiC from the OR of {10 0}$_α$ || {112}$_{TiC}$, corroborating the fact that α phase that nucleated from the TiB and the TiC does not have any relation with the β matrix. TiB and TiC particles share an OR of {101}$_{TiB}$ || {112}$_{TiC}$.
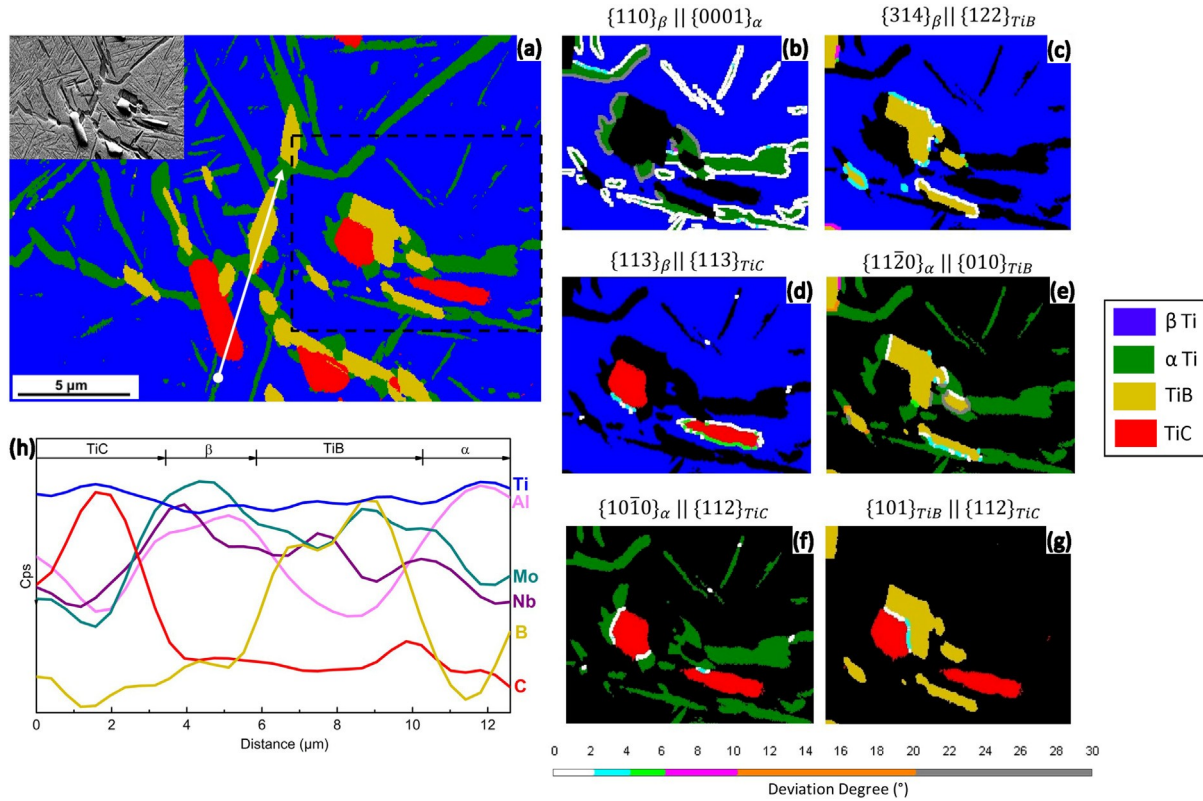

Fig. 5. (a) EBSD phase map of FC 0.5. Inset shows forescatter diode (FSD) image of region; (b–g) Deviation degree from the orientation relationship between all phases on the area designated in (a) by dashed lines; (h) EDS line scan of Ti, Al, Mo, Nb, B, and C of the white line displayed in (a).

Smoothed EDS line scan reveals the presence of the alloying elements is lower in TiC, while β has the largest concentration of Mo and Nb, followed by TiB, which has the lowest amount of Al, and finally α has more Al than all other phases. Silicon line is not shown due to low concentration and no considerable variation between phases.

Fig. 6 shows images of FC 1.5, where α is also not completely well indexed as the previous figure. There are few changes in the OR analysis, such as between β and TiB, that has now changed to {314}$_β$ ||{223}$_{TiB}$, which might be due to the larger size of TiB in comparison to borides in FC

0.5, and between α and TiB, with an OR of {10 0}$_α$ ||{100}$_{TiB}$. The same lack of relation between β and some of α that nu- cleated from TiB is also seen in this case, where the α with a gray line interface with β does not have any relationship with the cubic phase but has a good orientation relationship with TiB.
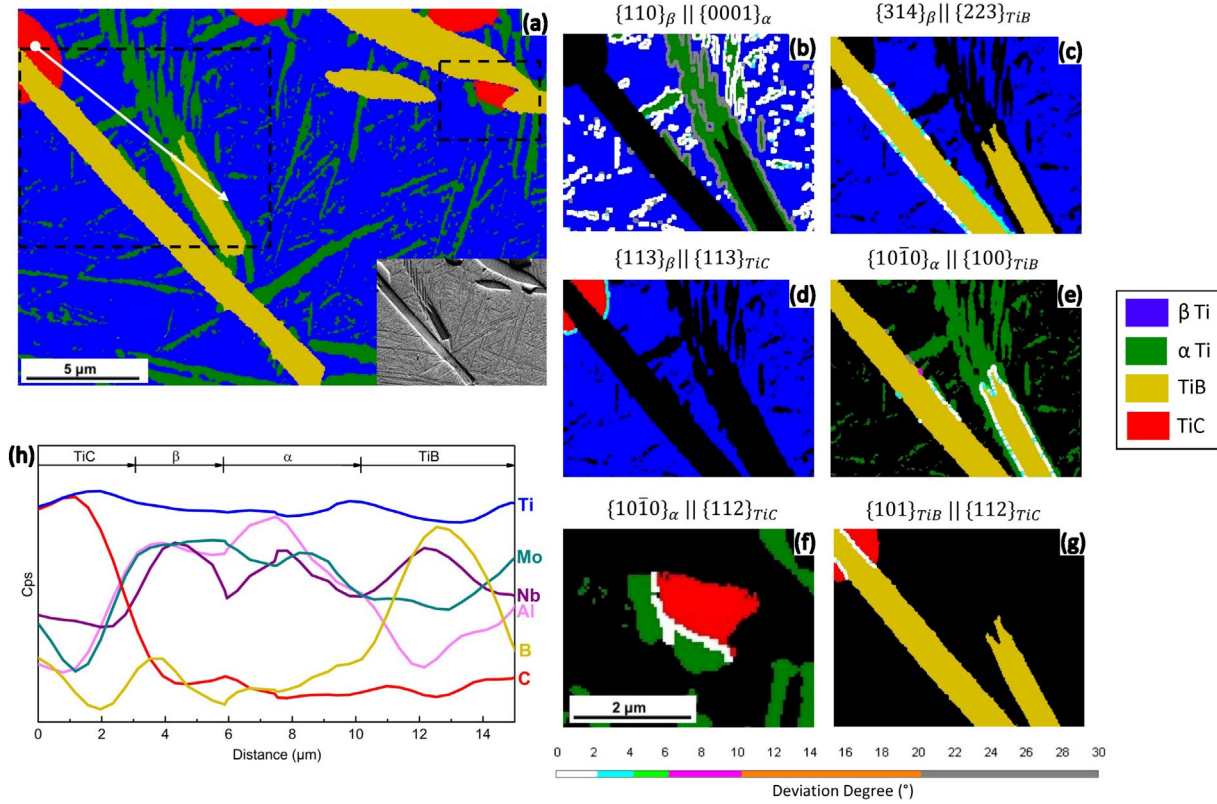

Fig. 6. (a) EBSD phase map of FC 1.5. Inset shows forescatter diode (FSD) image of region; (b–g). Deviation degree from the orientation relationship between all phases on the areas designated in (a) by dashed lines; (h) EDS line scan of Ti, Al, Mo, Nb, B, and C of the white line displayed in (a).

EDS lines keep the same trend as the previous composition, with low quantity of alloying elements in TiC, and α having the highest amount of Al which was probably rejected from TiB during heat treatment.

A clear difference in morphology of α can be identified both in Fig. 5 and Fig. 6, where those α phases away from TiB and TiC have in general a needle-like shape, while those α that have a proper OR with TiB and TiC seem to have irregular, non-acicular morphology.

Fig. 7 confirms that α could not be properly identified on this level of magnification in FC 3. The OR between β and TiB changes again to {110}$_β$ || {001}$_{TiB}$ [31] and between TiB and TiC to {123}$_{TiB}$ ||{101}$_{TiC}$, which might be due to the fact that in this composite, primary in-situ particles formed first from the liquid. In the images of OR be- tween β and TiB, and β and TiC, the deviation degree from the proposed orientation varies at the interface of the same particle. This is justified by the fact that the TiB and TiC particles are located on the grain boundaries, as seen

in the All Euler Map, and they will have a better OR with the β grains that have nucleated and grown from them.
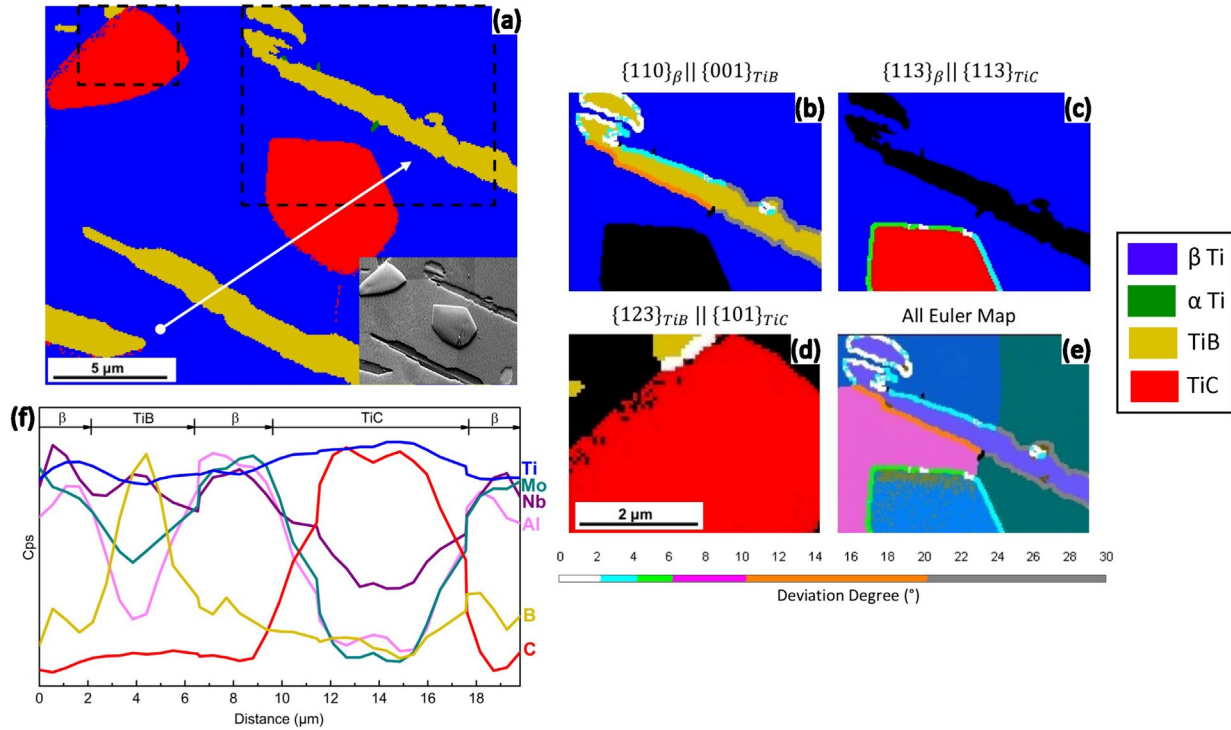

Fig. 7. (a) EBSD phase map of FC 3. Inset shows forescatter diode (FSD) image of region; (b–d). Deviation degree from the orientation relationship between all phases on the areas designated in (a) by dashed lines; (e) All Euler map showing the effect of a grain boundary in the modification of OR; (h) EDS line scan of Ti, Al, Mo, Nb, B, and C of the white line displayed in (a).

Fig. 8 and Fig. 9 show orientation images of selected regions from TEM of FC 3. In Fig. 8, irregular-shaped α (α_{center}) nucleates from TiB, while needle-like α (α_{top}) does not seem to have grown from the boride, instead, it has a good OR with the matrix of β. The region shown in Fig. 9 has all four phases, and α nucleates from both TiB (α_{top}) and TiC (α_{bottom}). Table 2 shows the OR between the phases, identified from the pole figures.

Most of the orientation relationships found through EBSD imaging have also been identified with TEM orientation imaging at an exact match or closely related.

3.3 Mechanical properties

Compressive strength increases with the addition of B_4C, as shown in Fig. 10. For the alloy without any addition of B_4C, compressive yield strength (CYS) and ultimate compressive strength (UCS) of 801 MPa and 1116 MPa were found, respectively, with a maximum deformation of 23.8%. With an increase in B_4C addition, ductility decreases for FC 0.5, to 14.6%, and FC 1.5 to 13.2% and increases again for FC 3, which might be due to a reduction in the volume of α, resulting in a β matrix with higher toughness. A CYS of 1055 MPa and UCS of 1521

MPa were found for FC 0.5, while a CYS of 1281 MPa and UCS of 1680 MPa were acquired for FC 1.5. The fact that an increased addition of B_4C to 3%, in FC 3, barely reduced the compressive yield strength and ultimate compressive strength to 1205 MPa and 1636 MPa, respectively, with a maximum deformation of 20.5%, makes this composite the one with the best ratio between stress-strain.
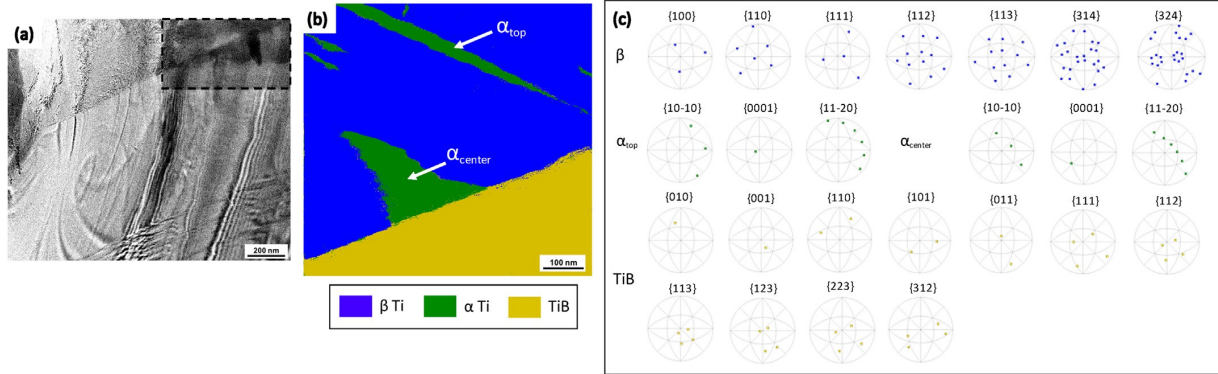

Fig. 8. (a) TEM bright field image of FC 3, showing a dashed line selected region where orientation imaging was carried out with ASTAR; (b) ASTAR orientation imaging showing phases present in selected region in (a); (c) Pole figures of each phase.
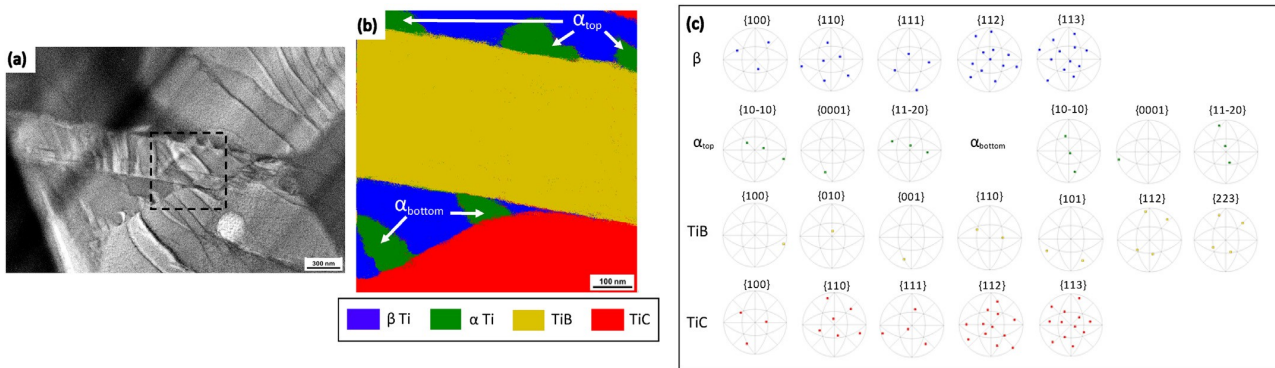

Fig. 9. (a) TEM bright field image of FC 3, showing a dashed line selected region where orientation imaging was carried out with ASTAR; (b) ASTAR orientation imaging showing phases present in selected region in (a); (c) Pole figures of each phase.

Hardness increases from FC 0 to FC 1.5, reaching a maximum of 424 HV for micro hardness and 460 HV for macro hardness, decreasing for FC 3 to 375 HV and 393 HV, for micro and macro hardness, respectively. The higher volume of β in FC 3 leads to a softer matrix, and even though this composite has a larger volume of hard TiB and TiC particles, the matrix impinges a stronger factor on hardness decrease.

Macro hardness tests with a load of 98 N results in higher hardness values for all materials in comparison to a lower load of 4.9 N in microhardness tests. In all cases, except for FC 1.5, macro and microhardness measurements are within each other's error bars.

Table 2 Orientation relationship between TiB, TiC, β, and α, verified from pole figures of ASTAR images of FC 3.

	TiB ∥ β	TiB ∥ α	TiB ∥ TiC	β ∥ α	β ∥ TiC	α ∥ TiC
Fig. 8	$\{111\}_{TiB} \parallel \{113\}_{\beta}$ $\{211\}_{TiB} \parallel \{314\}_{\beta}$ $\{211\}_{TiB} \parallel \{111\}_{\beta}$ $\{122\}_{TiB} \parallel \{314\}_{\beta}$ $\{223\}_{TiB} \parallel \{314\}_{\beta}$	$\{010\}_{TiB} \parallel \{10\bar{1}0\}_{\alpha}^{c}$ $\{223\}_{TiB} \parallel \{10\bar{1}0\}_{\alpha}^{c}$	–	$\{110\}_{\beta} \parallel \{0001\}_{\alpha}^{t}$ $\{111\}_{\beta} \parallel \{10\bar{1}0\}_{\alpha}^{t}$ $\{111\}_{\beta} \parallel \{11\bar{2}0\}_{\alpha}^{c}$	–	–
Fig. 9	$\{001\}_{TiB} \parallel \{110\}_{\beta}$ $\{101\}_{TiB} \parallel \{314\}_{\beta}$ $\{123\}_{TiB} \parallel \{324\}_{\beta}$ $\{210\}_{TiB} \parallel \{111\}_{\beta}$ $\{301\}_{TiB} \parallel \{314\}_{\beta}$ $\{321\}_{TiB} \parallel \{112\}_{\beta}$	$\{001\}_{TiB} \parallel \{0001\}_{\alpha}^{t}$ $\{010\}_{TiB} \parallel \{11\bar{2}0\}_{\alpha}^{t}$ $\{100\}_{TiB} \parallel \{10\bar{1}0\}_{\alpha}^{t}$ $\{210\}_{TiB} \parallel \{11\bar{2}0\}_{\alpha}^{t}$	$\{001\}_{TiB} \parallel \{100\}_{TiC}$ $\{211\}_{TiB} \parallel \{112\}_{TiC}$ $\{321\}_{TiB} \parallel \{113\}_{TiC}$ $\{101\}_{TiB} \parallel \{112\}_{TiC}$	$\{100\}_{\beta} \parallel \{11\bar{2}0\}_{\alpha}^{t}$ $\{110\}_{\beta} \parallel \{0001\}_{\alpha}^{b}$ $\{110\}_{\beta} \parallel \{0001\}_{\alpha}^{t}$ $\{110\}_{\beta} \parallel \{10\bar{1}0\}_{\alpha}^{t}$ $\{111\}_{\beta} \parallel \{11\bar{2}0\}_{\alpha}^{b}$ $\{112\}_{\beta} \parallel \{10\bar{1}0\}_{\alpha}^{b}$ $\{113\}_{\beta} \parallel \{10\bar{1}0\}_{\alpha}^{b}$	$\{110\}_{\beta} \parallel \{111\}_{TiC}$ $\{111\}_{\beta} \parallel \{110\}_{TiC}$ $\{112\}_{\beta} \parallel \{112\}_{TiC}$ $\{112\}_{\beta} \parallel \{113\}_{TiC}$ $\{113\}_{\beta} \parallel \{112\}_{TiC}$	$\{110\}_{TiC} \parallel \{11\bar{2}0\}_{\alpha}^{b}$ $\{111\}_{TiC} \parallel \{0001\}_{\alpha}^{b}$ $\{112\}_{TiC} \parallel \{10\bar{1}0\}_{\alpha}^{b}$

α^{t} - Alpha phase on the top of the ASTAR image (α_{top}).
α^{c} - Alpha phase on the center of the ASTAR image (α_{center}).
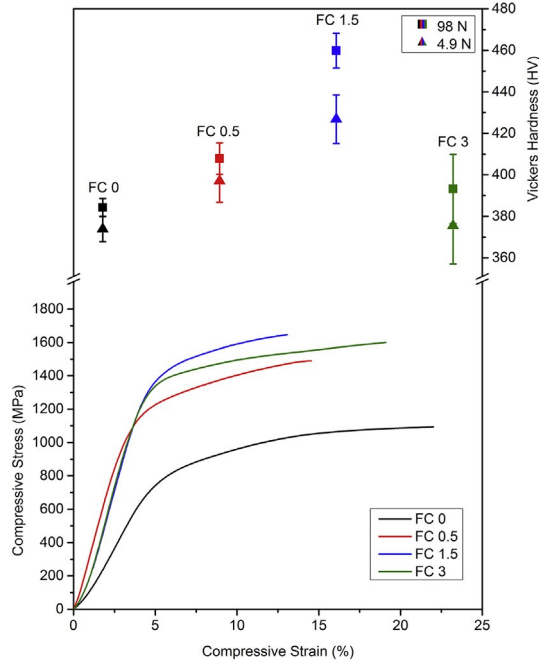α^{b} - Alpha phase on the bottom of the ASTAR image (α_{bottom}).

Fig. 10. Compressive stress-strain curve of fabricated materials, and Vickers micro (4.9 N) and macrohardness (98 N), with respective error bars.

Fig. 11 shows images of fractured regions of the samples subjected to compression tests. FC 0 samples have the coarsest α on the grain boundaries, which might explain the layered aspect in Fig. 11a, because the crack path would preferentially follow the grain boundaries. This material is the most ductile, which can be verified by the large presence of dimples in Fig. 11b. The featureless fractographs of FC 0.5 and FC 1.5, as seen in Fig. 11c and Fig. 11e, respectively, is a sign of the de- creased ductility of these samples, and the typical sliding of the surfaces in the oblique plane of the fracture, damaging the surface. Higher magnification in Fig. 11d shows intergranular fracture for FC 0.5, where the irregular shape of the smallest grains seems to be kept after fracture. For FC 1.5, as grains size are in the range of hundreds of microns, it is likely that the fractograph shown in Fig. 11f displays the inside of a grain where the intergranular fracture occurred and the tip of the crack followed a path from a cluster of particles to another. The low ductility of this material and the inherent scratching between the fractured surfaces may have removed features that would better explain the fracture mechanism. Fig. 11g and h, show the fractured region of the FC 3 sample, where a completely different structure is present. The

mixture of a ductile β matrix with coarse and extremely hard TiB e TiC particles cause a great number of fragments left all over the surface and ripped out particles leaving large cavities as the one in Fig. 11h.
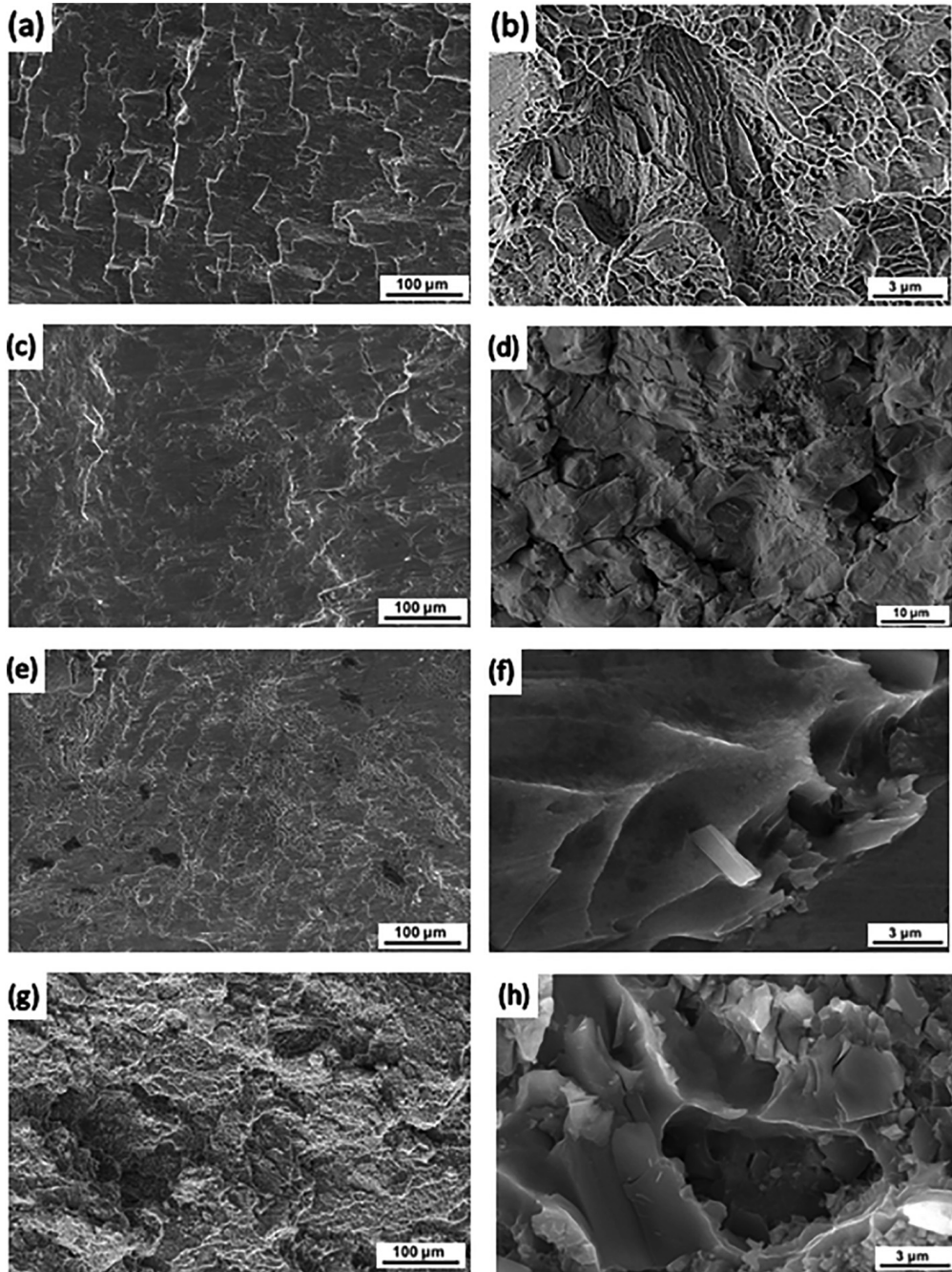

Fig. 11. SEM fractographs of Beta 21S alloy and composites. (a–b) FC 0; (c–d) FC 0.5; (e–f) FC 1.5; (g-h) FC 3.

4. Discussions

The significant increase in β stability resulting in finer α in the composites due to the addition of

B$_4$C and subsequent formation of TiB and TiC particles may have several reasons for taking place. A recent work developed by our group with the same materials used in the current paper showed that excess Ti is consumed during formation of the in-situ particles, making the matrix richer in solute elements such as Mo and Nb, as the volume of TiB and TiC increased [32]. A higher concentration of the aforementioned β-stabilizing elements could make the matrix more stable, causing a lower volume of phase transformation from β to α during slow cooling.

The effect of TiC in gettering oxygen from the matrix, especially those located at high free energy positions and atom mobility like the grain boundaries, could be another explanation for the increased β stability in FC 3, since oxygen is an α-stabilizing element [15].

Also, the fact that the content of Al, an α-stabilizing element, is low in TiB and TiC could explain why some α phase precipitated around these particles, as showed in the EBSD images. Al was most likely rejected from the TiB and TiC during solidification or during the furnace cooling in the heat treatment, remaining in the surrounding of these particles, and acting as a driver for the heterogeneous nucleation of α from them, as confirmed by the orientation relationship study.

Except by {001}$_{TiB}$||{100}$_{TiC}$ and {113}$_β$||{113}$_{TiC}$, all the orientation relationship found in the EBSD analyses were also confirmed by the pole figures from the ASTAR images. The irregular shape of α with complete OR with TiB and TiC clearly distinguishes itself from the needle-like α with perfect OR with the β matrix. The mentioned Al enrichment of regions around the TiB and TiC particles could be the main factor for the preferable formation of α with larger contact surface area instead of growing to more distant regions as a needle.

The grain refinement caused by the precipitation of the in-situ particles has already been demonstrated in the same materials in the as- cast condition [32]. The fact that the long heat treatment of 12 h at elevated temperature has not caused any significant change in grain size shows the effective restraining factor in grain boundaries movement imposed by the TiB and TiC particles.

The increase in mechanical strength of the composites in comparison to the alloy is a result of competing factors, as the greater the volume of TiB and TiC, the lower the volume and size of α. From the alloy to the composite with 3 wt% addition of B$_4$C, there is an increase in volume of TiB and TiC, which respond for an increase in strength due to the clean interface with the matrix acting as barriers for the move- ment of the tip of the crack during compression. While, the α phase, with its hexagonal close-packed structure also contributes to strengthening, but due to its gradual refinement from FC 0 to FC 3, its impact as a contributor to the materials strength is reduced. Mainly for FC 0.5 and FC 1.5, the combination of α + β in the matrix with increasing volume and size of TiB and TiC causes a great decrease in ductility and increase in strength, however, the extreme refinement of α in FC 3 improved ductility of the matrix maintaining the high strength due to the reinforcements.

For hardness, the great presence of phases homogenously distributed all over the matrix act as barriers for the movement of the geometrically necessary dislocations formed during indentation. The nanometric α present in FC 3 does not affect hardness as the α phase in other composites, so the soft β matrix absorbs any movement of the TiB and TiC when they are hit by the indenter.

5. Conclusions

The addition of different amounts of B_4C modified the micro- structure and consequently the mechanical properties of the developed composites. Thus, under the conditions of this study, the following conclusion can be drawn: (1) The melting arc process was sufficient to generate the in-situ TiB and TiC compounds from the boron carbide, and the amount of the compounds increased with the addition of B_4C, causing a refinement in α phase and changes in the needle-like morphology of α distributed in the matrix to irregular, non-acicular α shape around TiB and TiC; (2) Grain size decreased with increasing amount of B_4C, and (3) Increasing the amount of B_4C up to 1.5% in weight resulted in the highest values of mechanical strength and hardness, while higher fractions of boron carbide led to higher ductility and similar mechanical strength.

Declaration of competing interest

The authors declare that they have no known competing financial interests or personal relationships that could have appeared to influence the work reported in this paper.

References

[1] Bey Vrancken, et al., Microstructure and mechanical properties of a novel β titanium metallic composite by selective laser melting, Acta Mater. 68 (2014) 150–158, https://doi.org/10.1016/j.actamat.2014.01.018.

[2] Yang Jiao, Lujun Huang, Lin Geng, Progress on discontinuously reinforced titanium matrix composites, J. Alloys Compd. (2018), https://doi.org/10.1016/j.jallcom. 2018.07.100.

[3] Jinyong Zhang, et al., Microstructure and properties of in situ titanium boride (TiB)/titanium (TI) composites, Mater. Sci. Eng. A 648 (2015) 158–163, https://doi.org/10.1016/j.msea.2015.09.067.

[4] James D. Cotton, et al., State of the art in beta titanium alloys for airframe applications, Jom 67 (6) (2015) 1281–1303, https://doi.org/10.1007/s11837-015- 1442-4.

[5] Cherukuri Balakrishna, et al., The influence of trace boron addition on grain growth kinetics of the beta phase in the beta titanium alloy Ti–15Mo–2.6 Nb–3Al–0.2 Si, ScriptaMaterialia 60 (7) (2009) 496–499, https://doi.org/10.1016/j.scriptamat. 2008.11.040.

[6] T.T. Sasaki, et al., Nucleation and growth of α-Ti on TiB precipitates in Ti–15Mo–2.6 Nb–3Al–0.2 Si–0.12 B, Philos. Mag. 91 (6) (2011) 850–864, https://doi.org/10.1080/14786435.2010.533134.

[7] Agnieszka Szkliniarz, Microstructure and properties of Beta 21S alloy with 0.2 wt.% of carbon, Solid State Phenomena, 246 Trans Tech Publications, 2016, pp. 19–24, , https://doi.org/10.4028/www.scientific.net/SSP.246.19.

[8] Rajdeep Sarkar, et al., Crystallographic orientation relationships of boride and carbide particles with α and β phases in a β-Ti alloy, J. Alloys Compd. 612 (2014) 435–442, https://doi.org/10.1016/j.jallcom.2014.05.202.

[9] Banoth Ravinaik, et al., Effect of boron and carbon addition on microstructure and mechanical properties of metastable beta titanium alloys, Mater. Des. 67 (2015) 50–63, https://doi.org/10.1016/j.matdes.2014.11.004.

[10] R. Sarkar, et al., Effect of boron and carbon addition on microstructure and mechanical properties of Ti-15-3 alloy, Mater. Sci. Eng. A 528 (13–14) (2011) 4819–4829, https://doi.org/10.1016/j.msea.2011.03.014.

[11] L.-H. Chen, P.A. Blenkinsop, I.P. Jones, Effects of boron, carbon, and silicon additions on microstructure and properties of a Ti–15Mo based beta titanium alloy, Mater. Sci. Technol. 17 (5) (2001) 573–580, https://doi.org/10.1179/ 026708301101510230.

[12] D. Hill, et al., Formation of equiaxed alpha in TiB reinforced Ti alloy composites, ScriptaMaterialia 52 (5) (2005) 387–392, https://doi.org/10.1016/j.scriptamat. 2004.10.019.

[13] Wang Jiheng, et al., Morphology evolution of α phase in investment cast titanium matrix composites with B4C additions, J. Mater. Sci. 50 (17) (2015) 5674–5683, https://doi.org/10.1007/s10853-015-9120-z.

[14] Fengcang Ma, et al., Microstructure and mechanical properties variation of TiB/Ti matrix composite by thermo-mechanical processing in beta phase field, J. Alloys Compd. 695 (2017) 1515–1522, https://doi.org/10.1016/j.jallcom.2016.10.291.

[15] Z.Q. Chen, et al., Influence of 0.2 wt-% C on the aging response of Ti-15-3, Mater. Sci. Technol. 20 (6) (2004) 756–764, https://doi.org/10.1179/026708304225016806.

[16] R. Banerjee, et al., Direct laser deposition of in situ Ti–6Al–4V–TiB composites, Mater. Sci. Eng. A 358 (1–2) (2003) 343–349, https://doi.org/10.1016/S0921- 5093(03)00299-5.

[17] S. Tamirisakandala, et al., Grain refinement of cast titanium alloys via trace boron addition, Scriptamaterialia 53 (12) (2005) 1421–1426, https://doi.org/10.1016/j. scriptamat.2005.08.020.

[18] Sun Shuyu, et al., The influences of trace TiB and TiC on microstructure refinement and mechanical properties of in situ synthesized Ti matrix composite, Compos. Part B 43 (8) (2012) 3334–3337, https://doi.org/10.1016/j.compositesb.2012.01.075.

[19] M.J. Bermingham, et al., Effects of boron on microstructure in cast titanium alloys, ScriptaMaterialia 59 (5) (2008) 538–541, https://doi.org/10.1016/j.scriptamat. 2008.05.002.

[20] I. Weiss, S.L. Semiatin, Thermomechanical processing of beta titanium alloys—an overview, Mater. Sci. Eng. A 243 (1) (1998) 46–65, https://doi.org/10.1016/ S0921-

5093(97)00783-1.

[21]   H. Okamoto, C-Ti (carbon-titanium), J. Phase Equilib. Diffus. 19 (1) (1998) 89, https://doi.org/10.1007/s11669-006-5014-8.

[22]   J.L. Murray, P.K. Liao, K.E. Spear, The B—Ti (boron-titanium) system, Bull. Alloy Phase Diagr. 7 (6) (1986) 550–555, https://doi.org/10.1007/BF02869864.

[23]   S. Tamirisakandala, et al., Titanium alloyed with boron, Adv. Mater. Process. 164 (12) (2006) 41.

[24]   Chandran, K.S. Ravi, K.B. Panda, S.S. Sahay, TiBw-reinforced Ti composites: processing, properties, application prospects, and research needs, JOM 56 (5) (2004) 42–48, https://doi.org/10.1007/s11837-004-0127-1.

[25]   K. Morsi, V.V. Patel, Processing and properties of titanium–titanium boride (TiBw) matrix composites—a review, J. Mater. Sci. 42 (6) (2007) 2037–2047, https://doi.org/10.1007/s10853-006-0776-2.

[26]   K. Chaudhuri, J.H. Perepezko, Microstructural study of the titanium alloy Ti-15Mo-2.7 Nb-3Al-0.2 Si (TIMETAL 21S), Metall. Mater. Trans. A 25 (6) (1994) 1109–1118, https://doi.org/10.1007/BF02652286.

[27]   ASTM E9-19, Standard Test Methods of Compression Testing of Metallic Materials at Room Temperature, ASTM International, West Conshohocken, PA, 2019www. astm.org.

[28]   M. Imam, Study of transformation kinetics in Timetal-21 S titanium alloy, Titanium'95- Science and Technology, 1996, pp. 2361–2368.

[29]   H. Duschanek, P. Rogl, H.L. Lukas, A critical assessment and thermodynamic calculation of the boron-carbon-titanium (BC-Ti) ternary system, Journal of Phase Equilibria 16 (1) (1995) 46–60, https://doi.org/10.1007/BF02646248.

[30]   M.G. Glavicic, et al., Texture evolution in vacuum arc remelted ingots of Ti-6Al-4V, Mater. Sci. Eng. A 346 (1–2) (2003) 8–18, https://doi.org/10.1016/S0921- 5093(02)00525-7.

[31]   M. Ozerov, et al., Orientation relationship in a Ti/TiB metal-matrix composite, Mater. Lett. 186 (2017) 168–170, https://doi.org/10.1016/j.matlet.2016.09.124.

[32]   Vitor V. Rielli, Vicente Amigó-Borrás, Rodrigo J. Contieri, Microstructural evolution and mechanical properties of in-situ as-cast beta titanium matrix composites, J. Alloys Compd. 778 (2019) 186–196, https://doi.org/10.1016/j.jallcom.2018.11. 093.